J. Electrochem. Sci. Eng. **13(3)** (2023) 505-519; http://dx.doi.org/10.5599/jese.1610

Open Access : : ISSN 1847-9286
www.jESE-online.org

Original scientific paper

Modeling the velocity profiles in vanadium redox flow batteries-serpentine flow field

Sareda Yadav and Balaji Krishnamurthy✉

Department of Chemical Engineering, BITS Pilani, Hyderabad-500078, India

Corresponding author: ✉balaji.krishb1@gmail.com

Received: November 20, 2022; Accepted: January 28, 2023; Published: March 17, 2023

Abstract

A mathematical model is developed to study the effect of performance parameters on the velocity profiles in a vanadium redox flow battery. The effects of flow rate, viscosity, porosity, electrode thickness, and the effect of channel height on the velocity profile in a vanadium redox flow battery are studied. Quantitative analysis of velocity profiles at the mid-height of the channel, at the channel-electrode interface, and mid-height of electrode thickness is done. The channel height, thickness and porosity are found to have a substantial effect on the velocity profiles across the battery. It was found that the velocity at the electrode-channel interface is about three orders of magnitude lower than the velocity in the channels. Model results are compared with experimental data and found to agree well.

Keywords

Viscosity, porosity, channel height, channel width

Introduction

Because of global energy use and the issues of mitigating climate change, the number of energy storage devices for regenerative energy has steadily increased in recent years. On the other hand, renewable energy sources do not normally have a stable and immediate supply due to their intrinsically fluctuating nature, which leads to electricity grid destabilization [1]. As a result, deploying an effective and promising energy storage system (ESS) is necessary. In this respect, redox flow batteries (RFBs) have received great attention for ESS applications because of their flexible design, high efficiency, and long service life [2]. Vanadium redox flow batteries (VRFBs) are the most promising RFB technologies for large-scale energy storage [3]. The VRFB is an electrochemical device that stores energy in a vanadium-based electrolyte made by dissolving vanadium oxides or salts in sulfuric acid. Pumps transport the electrolytes from the reservoirs to the electrochemical cell or cell stack. At the anode and cathode, an ion exchange membrane separator allows protons to diffuse while preventing direct cross-mixing of electrolyte solutions from the two reservoirs in a typical cell.

A flow battery cell performance is influenced by two flow transport processes in particular. To begin with, the pressure drops necessary to move reactants across the system is an issue that affects the

system performance. Secondly, mass transfer to reaction sites on the surface of porous electrodes is directly influenced by the velocity distribution within a flow field and electrode. If a flow dead zone develops within a porous electrode, mass transport is limited to diffusion and migration. When compared to other places where reactants are actively supplied through convection, this can significantly reduce local current density. The pumped electrolyte flows through the electrode in a traditional flow battery since no flow channels are on the electrode felt. This could result in dead zones, bypassing, and unequal distribution of active species, resulting in a high concentration over-potential [4]. For a cell with flow fields, the use of channels can improve the flow distribution through the electrodes and lower flow resistance [5]. With a proper flow field design and low parasitic pumping loss, mass transport can be improved. Thus, the significance of reactant transport in flow batteries necessitates a thorough understanding of fluid flow within these cells.

Researchers have explored several flow parameters by creating a serpentine flow field (SFF), parallel flow field (PFF), and interdigitated flow field (IFF) in order to attain the aforementioned goals. Some research focuses on improving the VRFB performance by modifying battery materials, particularly electrode materials [6-8]. To provide uniform distribution of reactants in the porous electrodes, we must offer an acceptable flow field design. To increase the performance of VRFB, extensive research has been carried out to optimize the flow rate and flow field design. The majority of these researches are numerical simulations employing the mesoscopic lattice Boltzmann method [9,10] and macroscopic finite element method [11,12].

Xu *et al*. [13] compared the performance of VRFBs with and without flow field in their cell structure. They found that the VRFB with a flow field has a higher energy efficiency and a larger pressure drop than the VRFB without a flow field. Messaggi *et al*. [14] investigated interdigitated and serpentine flow field performance. According to their findings, the interdigitated flow field has a superior ability to uniformly transport the electrolytes, whereas the serpentine flow channels function better at significant pressure drops. Houser *et al.* [15] suggested various novel types of flow field designs and investigated performance and pressure drop under a variety of operating situations. Knudsen *et al*. [16] numerically investigated electrolyte flow and pressure drop in a wide range of designs of flow fields with porous electrodes. The results revealed that the design of flow fields for various area cells had a substantial impact on pressure drop and electrolyte distribution. On a cell active area of 5 cm^2 with serpentine flow design, the effect of electrolyte penetration into porous electrodes on battery performance was investigated by Ke *et al.* [17,18]. You *et al.* [19] investigated the design optimization of an interdigitated flow field. On a cell active area of 25 cm^2, Mayura *et al*. [20] investigated the effect of flow fields (interdigitated, multiple serpentines, and conventional) and electrolyte flow velocity on the performance of VRFB. According to their simulations, the electrolyte velocity in the electrode in SFF is an order of magnitude larger than in IFF. A few studies have reported on flow fields for large cell areas up to 900 cm^2 [19], 918 and 1495 cm^2 [21]. Stack findings for 1500, 1800, and 2714 cm^2 cells were reported by Li *et al.* [22], Wu *et al.* [23], and Park *et al*. [24], respectively. Irrespective of the flow field design, the uniformity of velocity distribution in the electrode is a critical parameter in limiting the electrochemical performance of VRFB cells. The majority of studies in the literature focused on the performance of VRFB batteries employing serpentine and other flow fields, carbon paper alone, and channel width and electrode thicknesses of less than 3 mm. They also reported velocity profiles in the middle of the channel and electrodes. It is also crucial to understand the distribution along the channel-electrode interface. Only few papers studied the effects of channel height, electrode thickness, porosity, and viscosity on velocity profiles. However, velocity profiles near the interface have not been studied

much in the literature. Since measuring experimental velocity profiles in the electrode and at the interface is challenging, there is no experimental data regarding velocity profiles in the literature. Computational fluid dynamics (CFD) simulations are used to study the velocity distribution in order to better understand it. In our research, we looked at velocity profiles near the interface and the impact of channel height, electrode thickness, porosity, and viscosity on velocity profiles in serpentine flow fields.

Modelling procedure

Model assumptions

The assumptions made in the three-dimensional model presented are given below.

1. The steady-state model, *i.e.*, time-variant phenomena are not taken into account.
2. An isothermal condition is assumed for all domains, *i.e.,* no temperature variation is taken into account.
3. The fluid flow is treated as incompressible flow.
4. The electrode and electrolyte are considered isotropic and homogeneous.
5. Effects from gravity are neglected.

Model equations and numerical simulations

COMSOL Multiphysics® software 5.3a with a free and porous medium flow module was used to forecast velocity profiles in the serpentine flow field. This module was created specifically for calculating fluid flow in porous medium and channels. The Brinkman equations were employed to depict the slower flow profile in a porous medium, whereas the Navier–Stokes equations were utilised to describe the fast flow profiles in the channel. Equations (2) and (3) show the Navier–Stokes and Brinkman equations, respectively. To get velocity distributions in the channels and porous electrode, the following mass and momentum conservation equations were solved.

- Continuity equation (1):

$$\rho \nabla u = 0 \tag{1}$$

- Navier Stokes equation in channels (2):

$$\rho(u\nabla)\, u = \nabla[-pI + \mu(\nabla u + (\nabla u)^T] + \mathbf{F} \tag{2}$$

- Brinkman's equations in porous media (3)

$$\rho(u\nabla)u = \nabla\left[-pI + \frac{\mu}{\varepsilon}\left(\nabla u + (\nabla u)^T\right)\right] - \left(\frac{\mu}{k} + \beta_F |u|\right)u + \mathbf{F} \tag{3}$$

The electrode is considered a porous media with a certain permeability (K) to calculate the pressure drop during flow through it. Darcy's equation (4) was used.

$$\Delta P_{\text{flet}} = \frac{\mu l Q}{KA} \tag{4}$$

The dependence of the permeability of a porous material on its porosity is often described by the Kozeny-Carman equation (5) [25] that is used by many authors in the literature [26,27].

$$k = \frac{d_f^{\,2}}{16K_{ck}} \frac{\varepsilon^3}{(1-\varepsilon)^2} \tag{5}$$

In the above equations, u represents the velocity of electrolyte flow, ρ represents the electrolyte density, ε denotes the porosity of the carbon felt electrode, μ represents the viscosity, β_F represents the Forchheimer drag coefficient, which was neglected in the present work, and **F** *is* volume force

vector, which is zero because gravity is not taken into account. k denotes the permeability of the porous electrode, d_f denotes fiber diameter, K_{ck} denotes the Kozeny-Carman constant.

There is very little research on the permeability of a conventional carbon fibre electrode. According to Gostick *et al*. [28], this value might be 0.1 μm^2, while Weber *et al.* [29] claimed 0.2 μm^2. Based on the compression of the electrode, several researchers have discovered that permeability values range from 0.119 to 0.75 μm^2 for various compression ratios [30].

The values of fibre diameter, porosity, and the Kozeny-Carman constant are substituted into equation (5) to calculate permeability in our model. All designs in this project employed a constant permeability of 0.033 μm^2. The values suggested for various simulation settings are listed in Table 1 and Table 2. With a relative tolerance of 0.001, the nonlinear iterative solver GMRES was used.

Table 1. *Geometrical and channel dimensions used in simulations*

Channel width, mm	Rib width, mm	Channel height, mm	No. of channels	Width of the electrode, mm	Length of the electrode, mm	Electrode thickness, mm	Active area, cm^2	No. of mesh elements
3	2.875	3	9	50	50	6	25	186649

Table 2. *Operating parameters used in simulations*

Paremeter	**Value**
Electrode length	50 mm
Electrode width	50 mm
Electrode thickness	6 mm
Channel size	2 and 3 mm
Density of electrolyte	1350 kg m^{-3}
Viscosity of electrolyte	0.005 Pa·s
Kazney-Carman constant	4.28
Carbon fiber diameter	17.6 mm
Porosity	0.7, 0.8, 0.9
Permeability	33 μm^2
Flow rate	30, 50, 70, 90, 110 ml min^{-1}

Boundary conditions

No-slip boundary criteria were applied to both channel and porous medium walls. A slip boundary condition is applied at the interface between channels and porous electrode surfaces. A flow rate was specified at the inlet. The pressure boundary conditions are established at the flow channel output, and the gauge pressure is 0 Pa.

Geometries used in simulations

The electrode utilised here has a 50×50 mm surface area and a thickness of 6 mm. The porous electrodes and square channels make up this shape. In these designs, channels are placed next to the porous electrode. Rib width refers to the distance between adjacent channels. Serpentine channel designs are with ratio of channel width to rib width is more than one. Figure 1 depicts the selected flow field geometry. The ratio of channel width to channel depth was kept constant throughout all simulations. The geometries, channel diameters, and rib-width details are shown in Table 1.

Meshes

Meshes for the flow design with a 3 mm channel width were created using COMSOL Multiphysics software version 5.3a. There are 186649 mesh elements in total. Tetrahedral pieces make up the majority of the mesh in flow designs, seen in (Figure 1b).

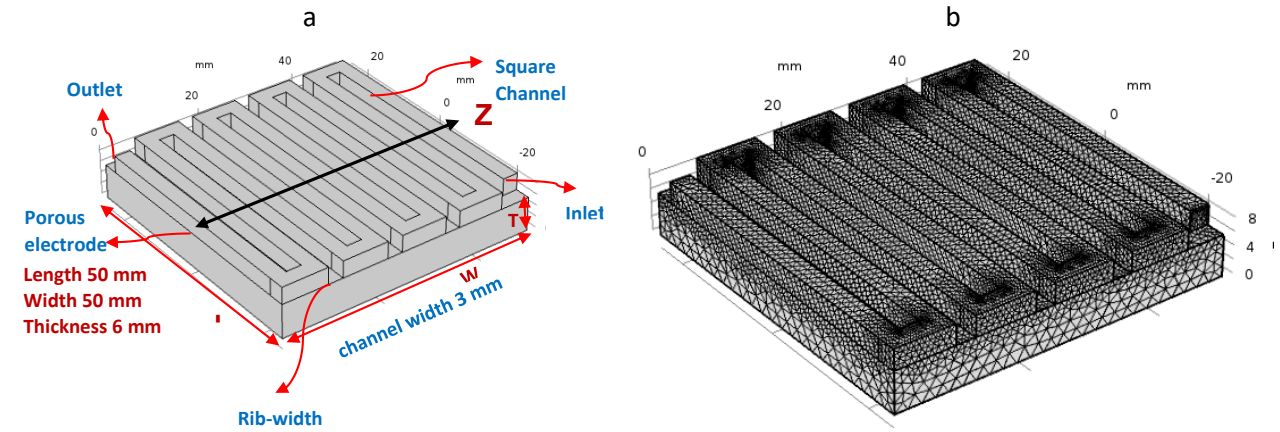

Figure 1. *(a) Schematic diagram of the serpentine flow field and (b) meshes used in simulations*

Results and discussion

Effect of flow rate on velocity profiles

We employed flow designs with a ratio of channel width to rib width of 1.043 to investigate the effect of flow rate. The channel depth is equal to the channel width. Flow rates range from 30 to 110ml min^{-1}, with a 20 ml min^{-1} step size. Tables 1-2 contain all geometric details and simulation parameters. The flow distributions are depicted as velocity magnitudes based on CFD simulations of flow *via* serpentine channels attached to graphite electrodes. The velocity contours for the 25 cm^2 active area cell at 90 ml min^{-1} are shown Figure 2.

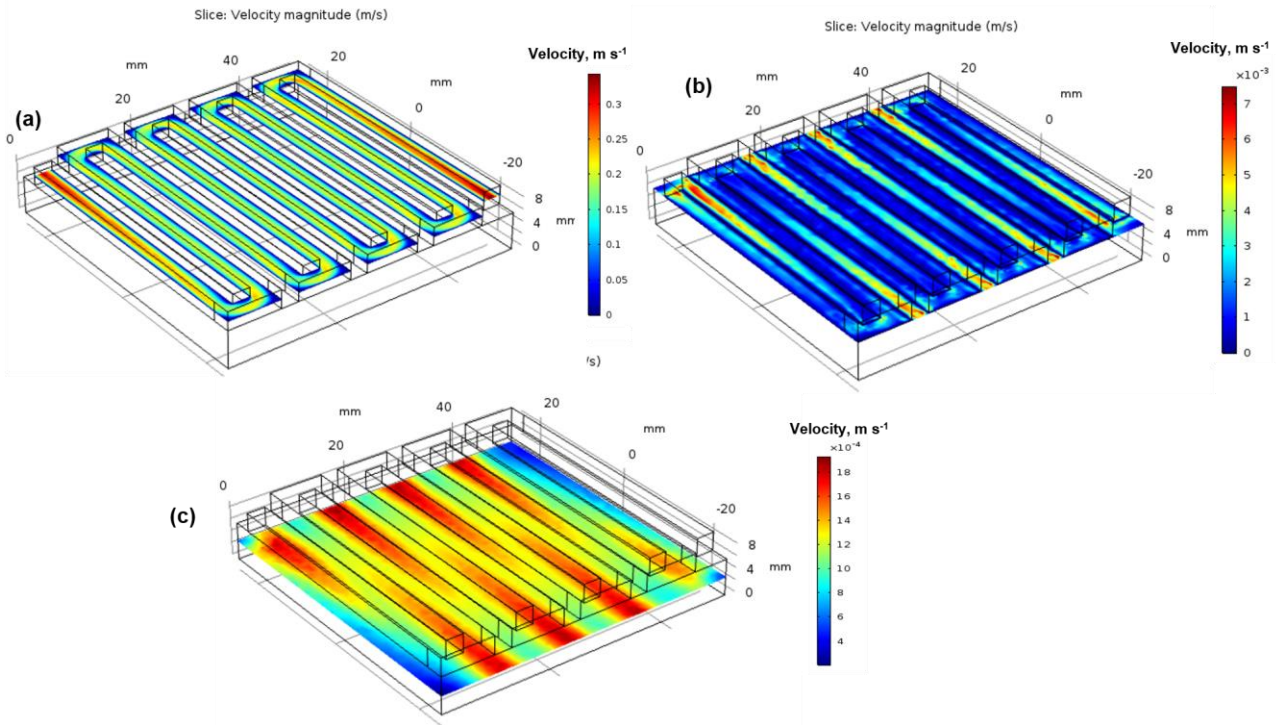

Figure 2*. Velocity contours in a serpentine flow field for a - channel middle, b - interface and c - electrode middle*

The predicted velocity contour planes are obtained in the middle of the channels, at the interface, and in the middle of the electrode, and the results are shown in Figure 2. As is typical of laminar flow in rectangular cross-section channels, the channel velocity is higher towards the entry and outlet, as well as in the channel centre (Figure 2a). The electrode-channel interface has a velocity

that is about three orders of magnitude lower than the velocity in the channels due to the porous medium flow characteristics (Figure 2b). With more fluid flow inside the porous media, we may see a 4-order of magnitude decrease in velocity compared to velocity in the channels. Due to pressure dips along the channels and fluid being urged to flow through the electrode towards downstream channels, the electrode velocity is highest in places not directly beneath the flow channels.

The influence of flow rate on velocity profiles is investigated by altering flow rate and plotting graphs in the middle of the channel (along the Z line shown in Figure 1), at the interface, and in the middle of the electrode. Figure 3 shows the corresponding results.

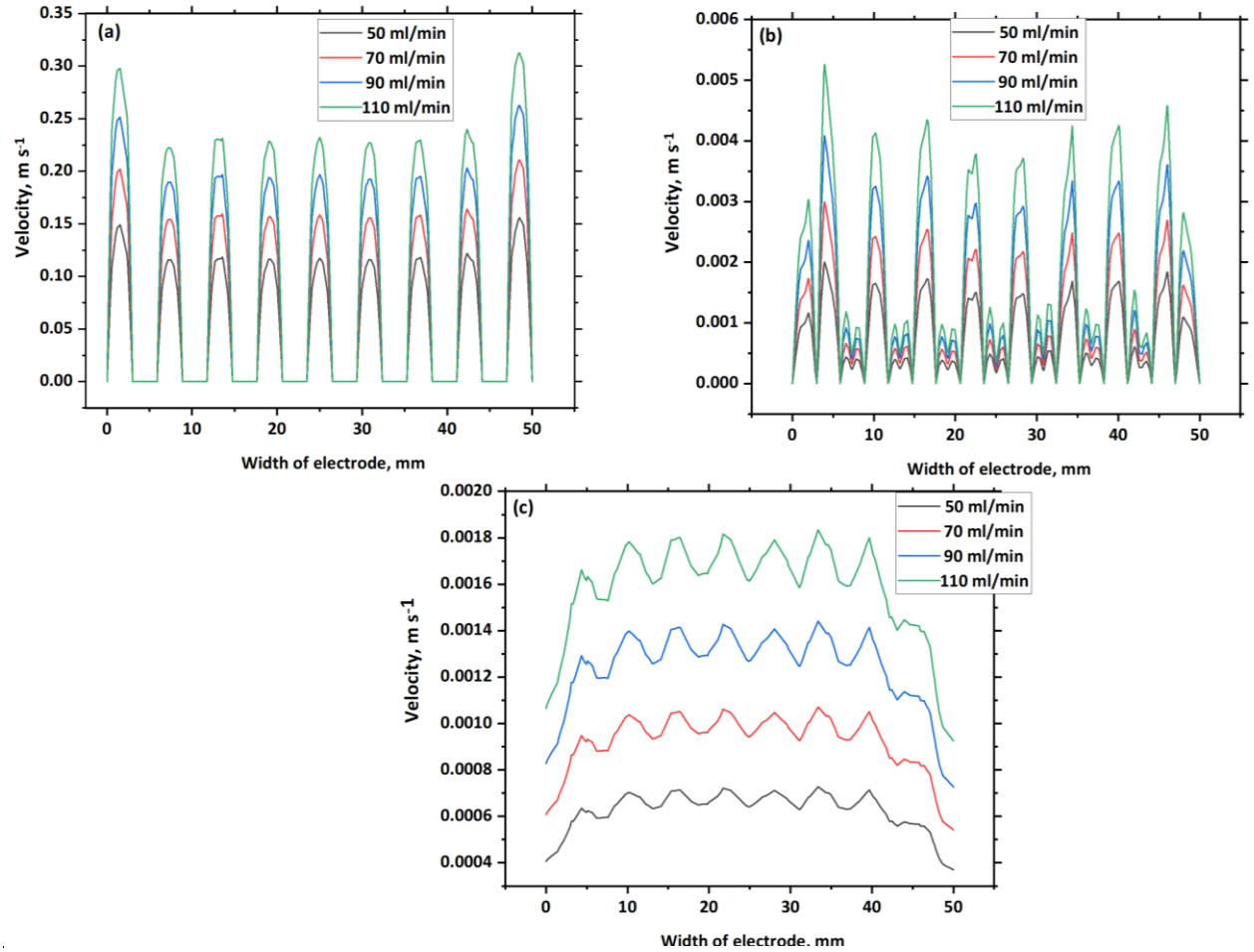

***Figure 3**. Effect of flow rate on velocity profiles in a serpentine flow field for (a) channel middle, (b) interface, and (c) electrode middle*

It can be seen that the anticipated velocity in the second and following parallel channels is slightly lower than that in the inlet channel and that the successive channels in between the inlet and outlet channels have a more uniform parabolic velocity distribution with a smaller magnitude (Figure 3a). This is due to the crossflow across the porous medium. Another observation is that the intensity of velocity magnitude peaks rises as the flow rate increases. We can also see minor velocity magnitude peaks under the rib region, indicating that crossflow is occurring beneath the ribs (Figure 3b). The velocity profiles drawn at the electrode midpoint are shown in Figure 3c. The velocity distribution exhibits oscillatory behaviour with a mean amplitude of 0.0013 m/s across the entire length for a flow rate of 90 ml/min and lesser values for low flow rates.

Effect of channel height on velocity profile

Channel heights were varied from 1 mm to 4 mm to investigate the influence of channel height. Flow designs with a ratio of channel width to rib width of 1.043 were chosen. Tables 1-2 contain all other simulation settings. The thickness of the electrodes is kept constant at 6 mm. For a flow rate of 90 ml/min, Figure 4 shows the effect of channel height on velocity profiles along the mid-plane of the channel, at the interface, and in the mid-plane of the electrode. The anticipated velocity profiles reveal that as channel height increases, the peak intensity of velocity decreases. This is because the pressure loss increases as the channel height decreases. When the depth of a channel is increased while the width remains constant, the hydraulic diameter of the channel increases, giving the fluid greater space to flow through it. As a result, the pressure drop is significantly reduced. In serpentine channels, pressure drop and velocity profiles are directly related. The velocity through the serpentine flow field decreases from inlet to outlet (Figure 4a) with increasing in channel height. Similar observation also seen in Figure 4b is a decrease in velocity with an increase in channel height, but a decrease in velocity magnitude is more at the interface compared to channels. Except for the initial and last flow passages with higher velocity, the velocity profiles are nearly consistent across the breadth of the cell. Except for relatively modest fluctuations related to local convection from the channel to the porous substrate and *vice versa*, which exhibit oscillatory behaviour, the velocity distribution in the electrode felt is uniform (Figure 4c). The electrolyte velocity in the electrode is significantly lower than that in the channels, as seen in Figure 4c.

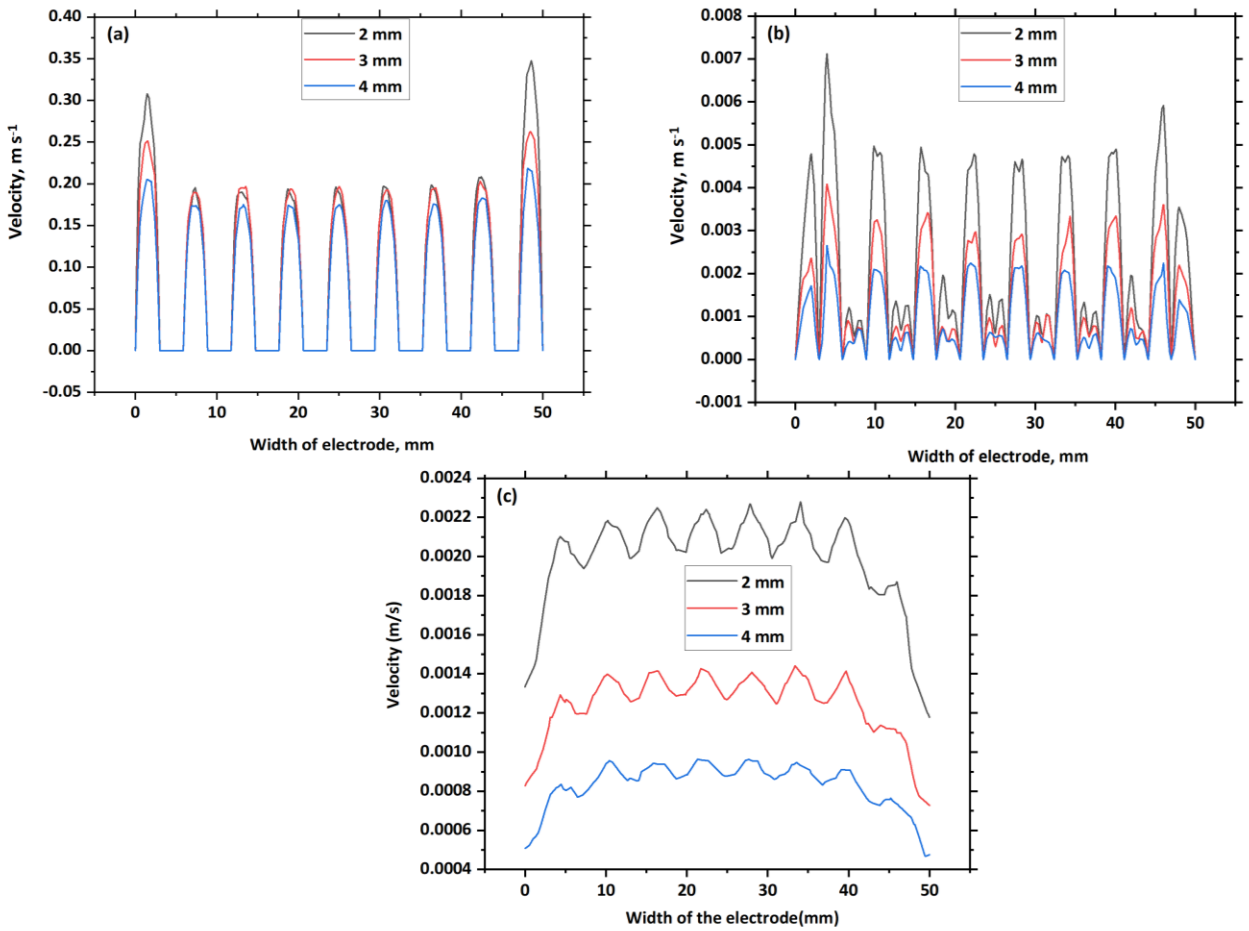

Figure 4. *Influence of channel height on velocity profiles in a serpentine flow field for (a) channel middle, (b) the interface and (c) the electrode middle*

Effect of electrode thickness on velocity profile

The thickness of an electrode has the greatest impact on both voltage efficiency and pumping power, and it should be considered from the beginning of the system design. Flow batteries frequently employ carbon felt as an electrode. The thickness of this felt is usually between 1.5 and 8 mm [31]. The influence of porous electrodes with four different thicknesses, namely 2, 4, and 6 mm, on velocity profiles in a serpentine flow field was investigated in this work. For a channel width of 3 mm, Figures 5a and 5b show the effect of electrode thickness on velocity distribution contours. These contour planes are shown for electrode thicknesses of 2 mm (Figure 5a) and 3 mm (Figure 5b) at the interface. As indicated in Figure 5b, the lowest velocity magnitude is recorded for the electrode thickness of 3 mm. According to Darcy's law, the pressure drop through the electrode is proportional to the electrode length (*L*) and inversely proportional to the electrode thickness, as shown in equation (4). Similarly, Figure 5c and Figure 5d show the mid of electrode contour planes for thicknesses of 2 mm and 3 mm, respectively. As demonstrated in Figure 5d, the velocity magnitude is smaller in the case of thickness 3mm than in the case of thickness 2mm, but the intensity of the velocity distribution increases and dead zones decrease. When the electrolyte flows from the interface to the centre of the electrode, the same behaviour is observed.

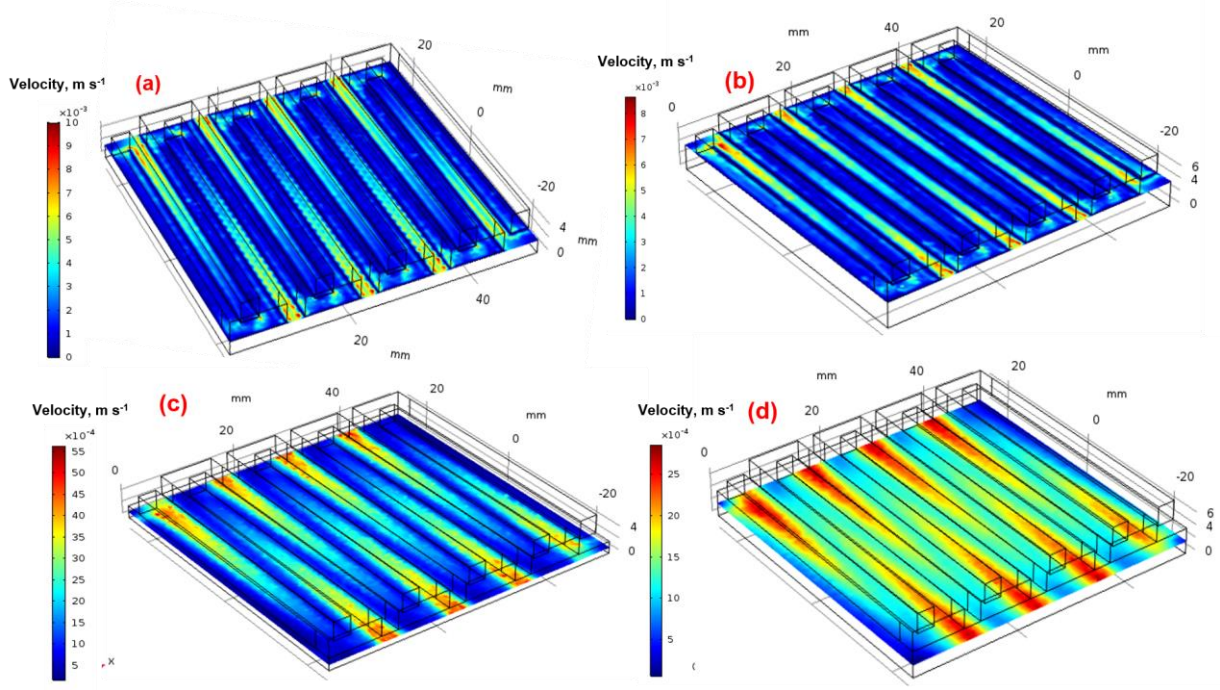

Figure 5*. Velocity contours in serpentine flow field for electrode thicknesses of 2 and 3 mm: (a) and (b) at the interface, (c) and (d) in the middle of the electrode*

Figure 6a shows predicted velocity profiles along the centreline in the width direction for electrode thicknesses of 2 mm, 4 mm, and 6 mm at mid-flow field height, at the interface in Figure 6b, and at mid-electrode depth in Figure 6c. The profiles were collected at a flow rate of 90 ml/min. The larger velocity magnitude is observed in the inlet and gradually diminishes as it goes through the successive channels, maintaining a uniform magnitude before reaching the outflow. The parabolic profiles are shown in the centre of the channels. Another finding is that velocity reduces as electrode thickness increases, as illustrated in Figure 6a. As illustrated in Figure 6b, crossflow velocities emerge under the rib region, and the intensity of the velocities diminishes as the thickness increases. The velocity profiles at the mid of the electrode are given in Figure 6c, and it can be seen that the velocity stability increases as the electrode thickness increases while the velocity magnitude drops.

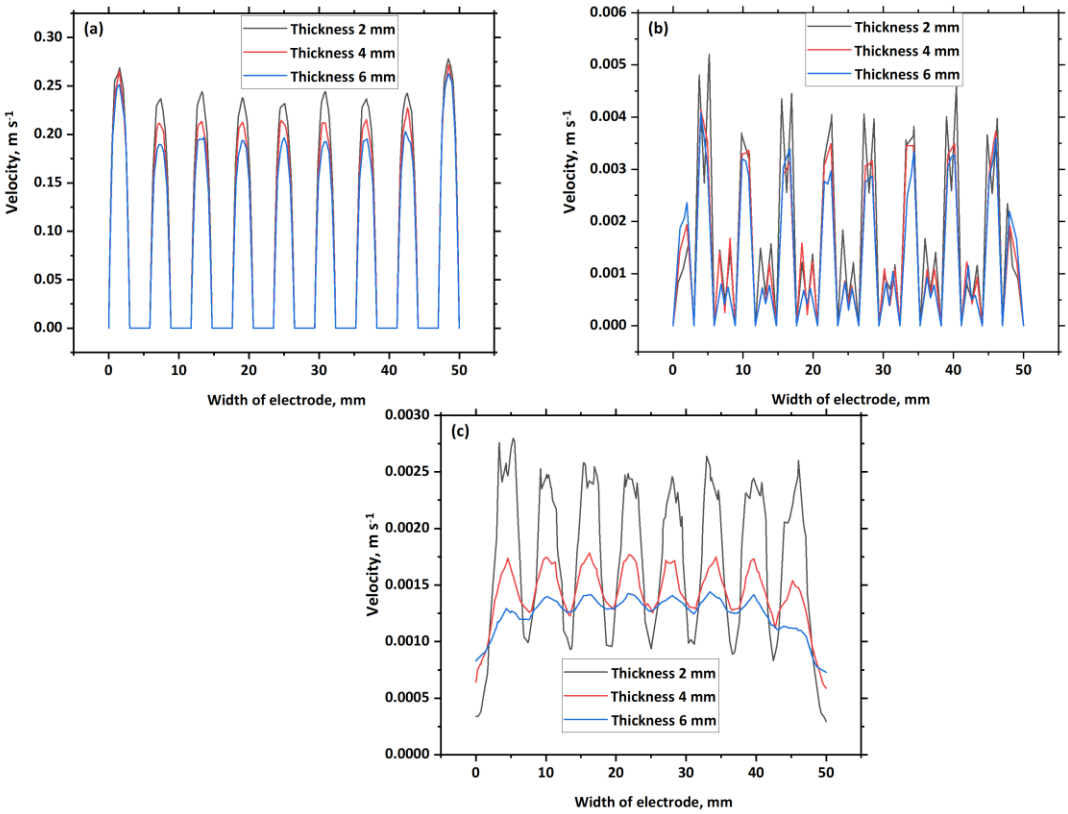

***Figure 6**. Influence of electrode thickness on velocity profiles in a serpentine flow field for (a) channel middle, (b) the interface, and (c) the electrode middle*

Effect of porosity

We used the simulation parameters listed in Tables 1-2 in the following research. The heights of the channels are the same as the widths of the channels. The thickness of the electrode is 6 mm. The effect of porosity is studied by varying porosities 0.7. 0.8 and 0.9 and corresponding permeabilities are 0.172, 0.5792 and 0.330 μm^2, respectively. The effect of porosity is studied using the above permeability values in the following section. Figure 7 shows the effect of porosity on velocity distribution contour planes obtained in the centre of the channel, at the interface, and in the middle of the electrode for a 90 ml min^{-1} flow rate. Figure 8 shows corresponding velocity profiles at the same locations. The flow enters the serpentine channel and splits among many parallel pathways before reuniting to emerge via the outlet. This is shown in Figure 7 in the form of velocity magnitude contour plots in Figures 7a and 7b for porosities 0.7 and 0.8, respectively. For porosity 0.7, the magnitude of velocity contours is greater than for porosity 0.8. The velocity changes are confined to flow channels due to the wall effect, and the flow distribution is uniform across the cross-sectional area of the whole channel. The velocity at the interface is higher for porosity 0.8 (Figure 7d) than for porosity 0.7 (Figure 7c). This is because if the porosity is too low, the flow penetration through the electrode will be low, which will result in poor cell performance. It also raises the impedance to electrolyte flow. The contour planes of velocity magnitude taken at the electrode midpoint are shown in Figures 7e and 7f. In comparison to porosity 0.7, the velocity for porosity 0.8 (Figure 7f) is higher than porosity 0.7 (Figure 7e). This is owing to the fact that when porosity increases, permeability also increases, which leads to an increase in velocity magnitude. We can also see that as velocity increases, the uniform velocity distribution increases and the number of dead zones reduces. The performance of the battery will improve owing to this.

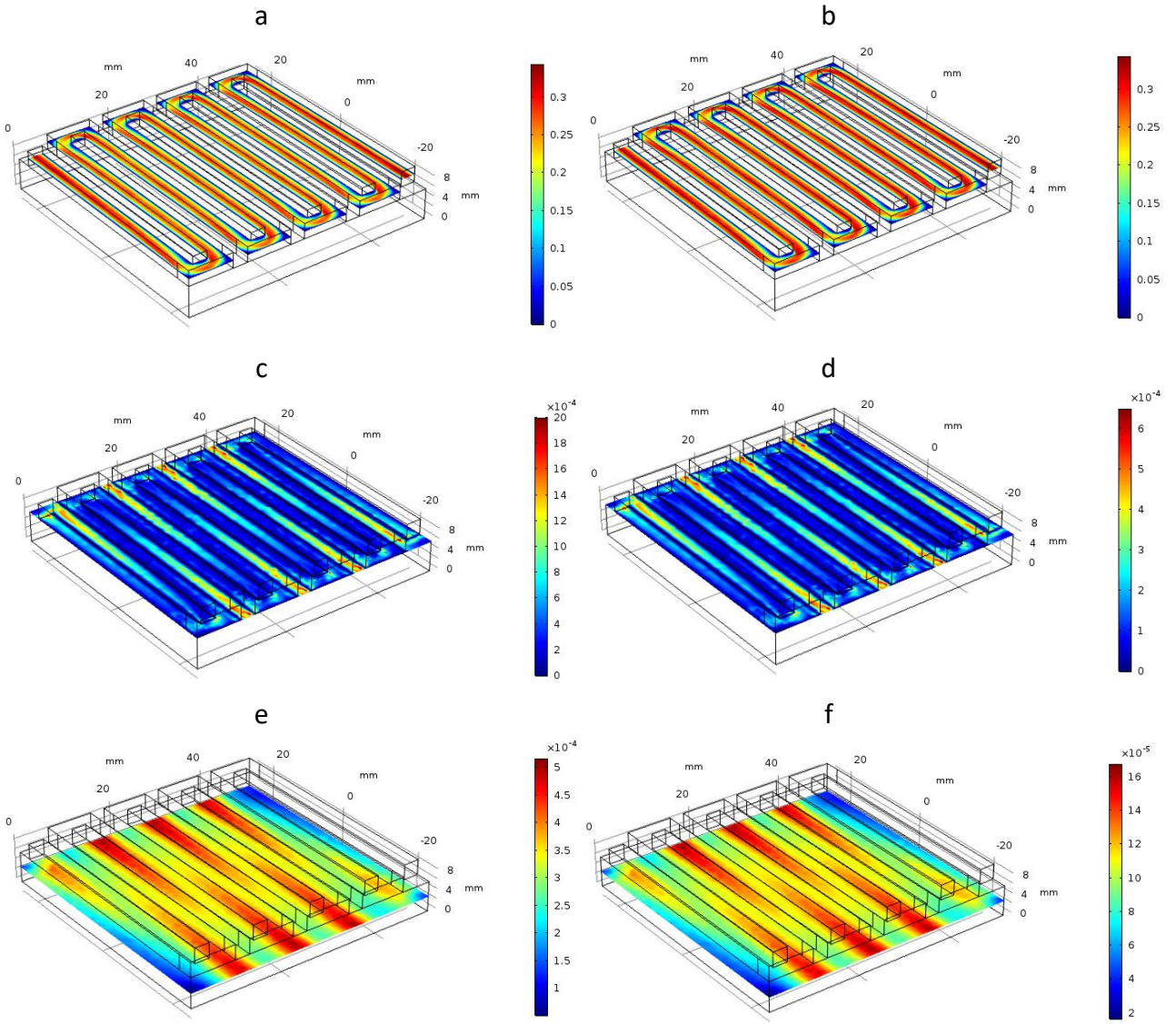

Figure 7. *Effect of porosity on velocity contours in a serpentine flow field for porosity 0.7 and 0.8 for (a) and (b) in the mid of the channel, (c) and (d) at the interface, (e) and (f) in the middle of the electrode. Colorbar: Velocity, m s^{-1}*

The influence of porosity on velocity profiles can be evaluated quantitatively. Figure 8 shows the profiles collected in the middle of the channel, at the interface, and in the middle of the electrode for a flow rate of 90 ml min^{-1}. The magnitude of the velocity is shown to be greatest for a porosity of 0.7 and lowest for porosity of 0.9. The flow along the channels in SFF (Figure 8a) fluctuates in direction but is usually uniform over the width. The velocity at the interface is higher for porosity 0.9 than for porosity 0.7 (Figure 8b). When compared to the velocity through the channel, the velocity distribution in the electrode is two orders of magnitude lower. This is owing to the significant influence of porosity. The velocity profiles taken at the middle of the electrode are shown in Figure 8c. The velocity appears to rise as the porosity increases.

Effect of viscosity on velocity profiles

We used the simulation parameters listed in Tables 1-2 in the following study. The height of a channel is the same as its width. The thickness of the electrode is 6 mm. For a 90 ml min^{-1} flow rate, the effects of viscosity on the velocity distribution profiles taken in the centre of the channel, at the interface, and in the middle of the electrode are shown in Figure 9.

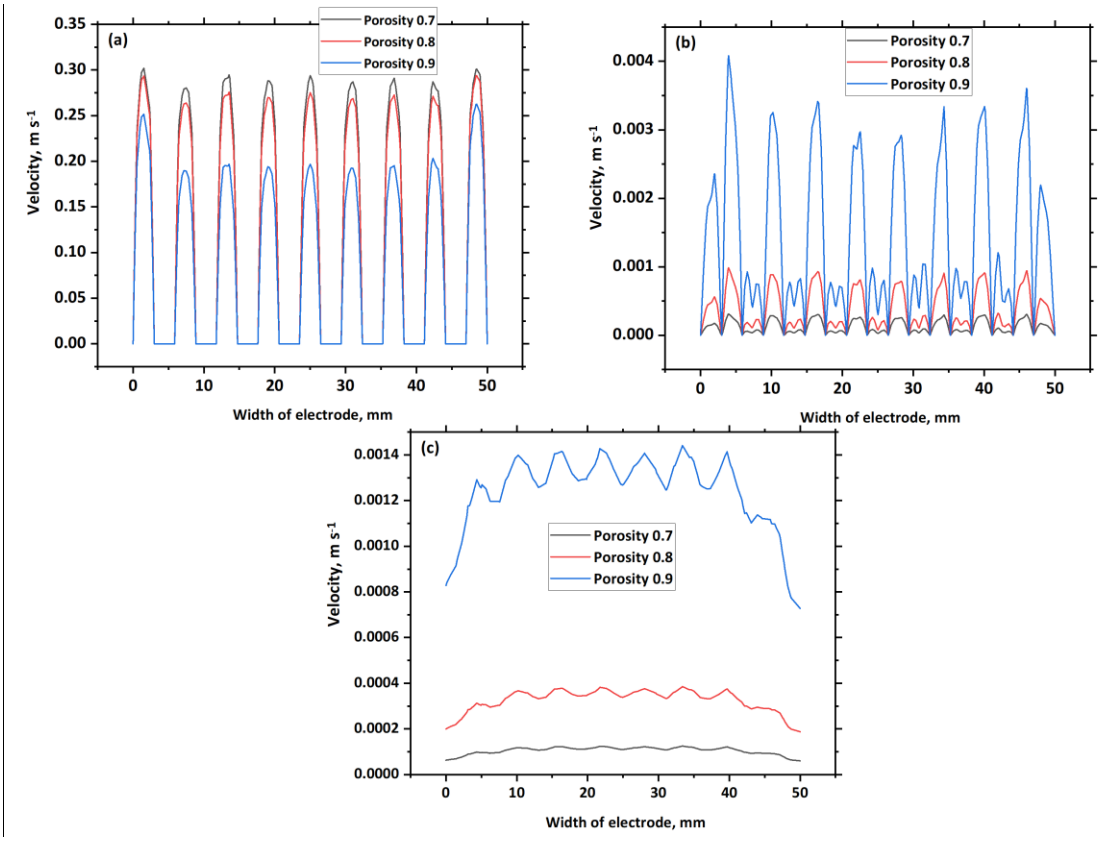

***Figure 8**. Influence of porosity on velocity profiles in a serpentine flow field for electrode thickness of 6 mm for (a) channel middle, (b) the interface, and (c) the electrode middle*

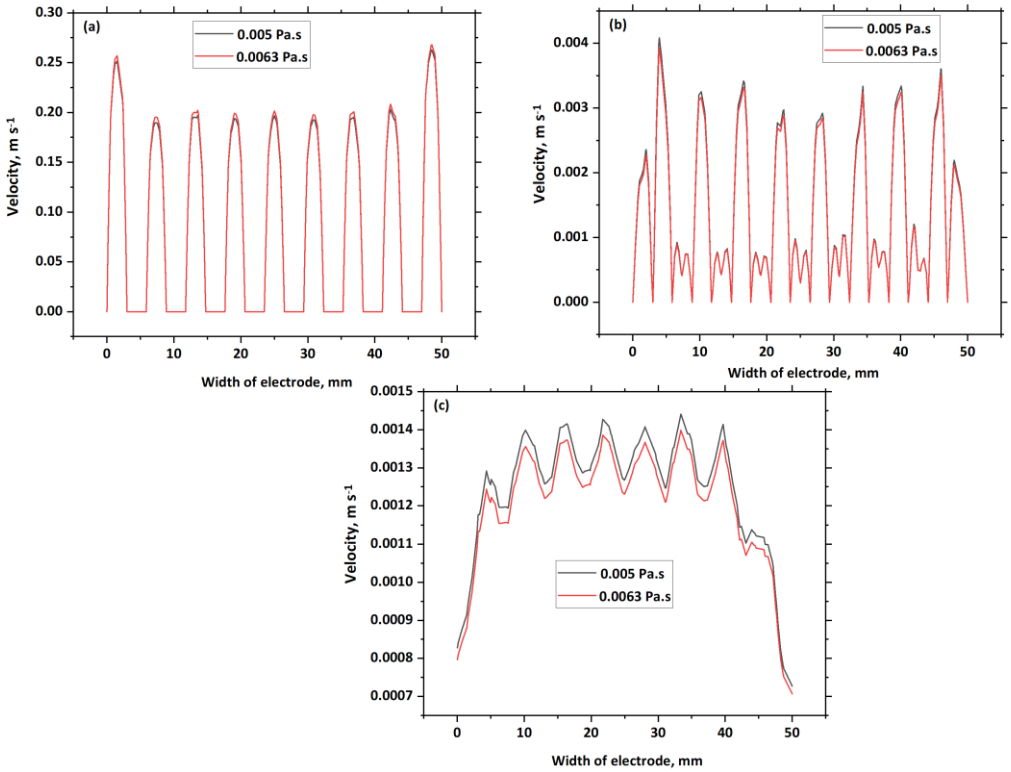

***Figure 9**. Effect of viscosity on velocity profiles in a serpentine flow field for (a) channel middle, (b) the interface, and (c) the electrode middle*

It is noted that velocity is higher in the input channel and drops as it advances toward the channel outlet. Between the channel inlet and outlet, the velocity profile follows the same pattern. As shown

in Figure 9a, the intensity of the peak of velocity profiles increases as the viscosity of the electrolyte in the channel increases. This is because velocity is affected not only by pressure drop and permeability, but also by fluid viscosity. Increased viscosity increases flow resistance in a porous material and channel flow, resulting in increased pressure drop. Pressure losses will also be driven by higher viscosities, but only with a sub-linear viscosity scaling.

When we compare velocity profiles to channels at the interface, we see that they behave differently. Figure 9b shows the crossflow velocity under the rib section.

The velocity profiles taken at the middle of the electrode are shown in Figure 9c. The magnitude of the velocity reduces as the viscosity increases, and this effect becomes more pronounced as the fluid flows deeper into the electrode. This is owing to the increased flow resistance of the fluid.

Comparison of modeling results with experimental data

Experimental values for the velocity field are not available in the literature, and it is very challenging to measure velocity profiles at the interface and in the electrode. As a result, we are unable to make a comparison between simulated and experimental velocity profiles. Therefore, we compared simulation results to experimental data of pressure drop available in the literature for serpentine flow fields. The schematic diagram and geometric details of a serpentine flow field are shown in Figure 10, which is composed of squared channels (equal channel width and channel height) placed on the top of the electrode.

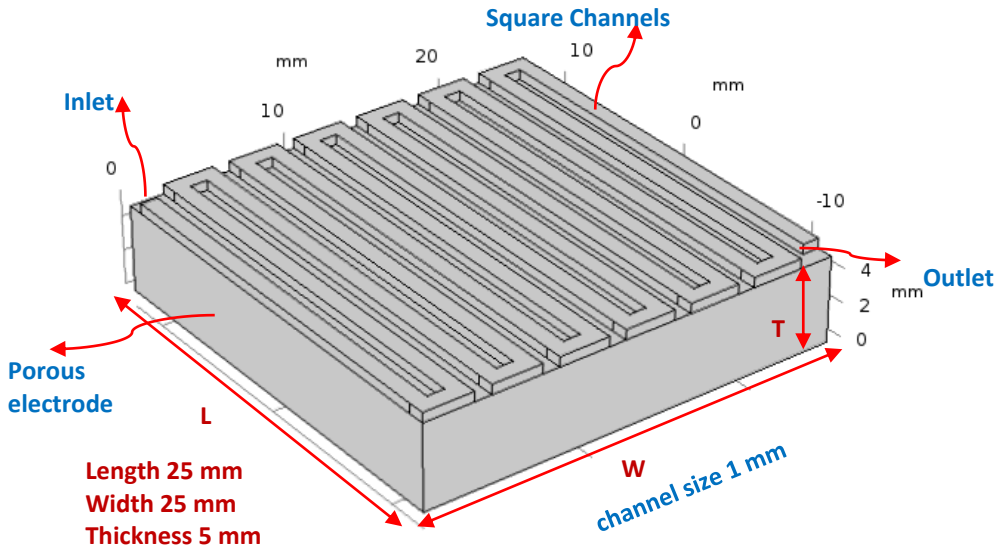

***Figure 10**. Schematic diagram of the serpentine flow field configuration studied for validation*

The electrode active area is 25×25 mm. Each flow field consists of flow channels with a cross-sectional area of 1×1 mm (channel width and height) and a rib width of 1 mm between them. The original thickness of the carbon felt was 2.5 mm. We used two layers of carbon felt and kept the experiment in the same conditions. In our simulation, we assume the channel height will be reduced by 58 %. The pressure drop between the cell input and output was measured using water (density and viscosity similar to the electrolytes used in VRFBs) flowing through the flow field at inlet Reynolds numbers ranging from 0 to 1720. Density and viscosity of water are assumed to be 998.2 kg/m^3 and 0.001003 Pa·s, respectively because it is the working fluid. Simulation was carried out in the same way as the experiment [30]. The experimental data [30] validates the numerically expected pressure reduction in a serpentine flow field. The operational conditions were set to match those of the experiment. Figure 11 depicts the comparison of numerical and experimental results.

In Figure 11, it can be observed that the numerical model accurately matches the trend using experimental data at low flow rates. The permeability values were obtained from the literature [31-34].

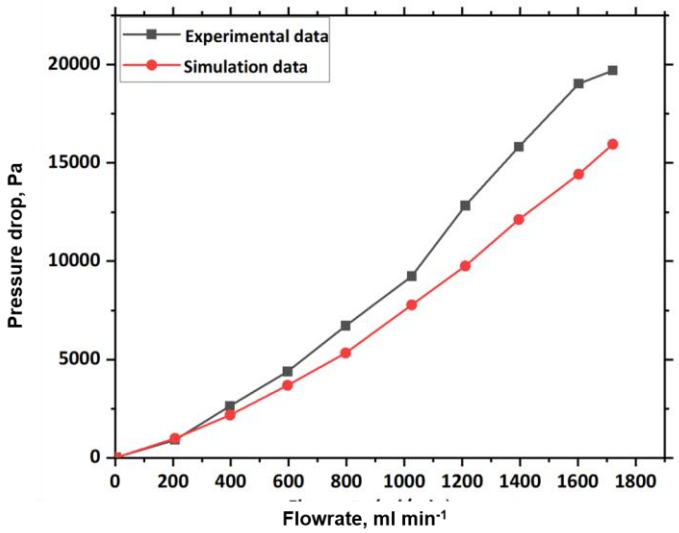

Figure 11. *Comparison of experimental and numerical data of pressure drop in serpentine flow field [30]. Permeability 0.75 μm^2*

Conclusion

A mathematical model is developed to study the effect of operating and design parameters on the velocity profiles in a vanadium redox flow battery under serpentine configuration. Simulation results showed that with reduced channel depth, the velocity profiles of the redox liquid are enhanced. On similar lines increasing flow rates, reduced electrode thickness and increasing porosity of the electrodes enhance the redox liquid velocity profiles. This can enable the reduction of stagnant zones in the battery and in the electrode, enhancing battery performance. Since experimental values of the velocity profiles in the battery are not available in the literature, pressure drop *versus* flow rates (experimental *vs*. theoretical) was compared and found to agree well.

Nomenclature

u	Velocity of electrolyte flow, m/s	L	Length of the electrode
ρ	Electrolyte density, kg m^{-3}	W	Width of the electrode
p	Pressure of the fluid, Pa	T	Thickness of the electrode
ε	Porosity	∇	Del operator
μ	Viscosity, Pa·s	RFB	Redox flow batteries
β_F	Forchheimer drag coefficient	VRFB	Vanadium redox flow battery
F	Volume force vector, N	ESS	Energy storage system
k	Permeability	SFF	Serpentine flow field
K_{ck}	Kozeny-Carman constant	PFF	Parallel flow field
d_f	Fiber diameter	IFF	Interdigitated flow field

Acknowledgement: *We wish to acknowledge the DST Research grant CRG/2021/000060-C and BITS Pilani, Hyderabad for providing the required support to publish this paper.*

References

[1] H. Ibrahim, A. Ilinca, J. Perron, *Renewable and Sustainable Energy Reviews* **12** (2008) 1221–1250. https://doi.org/10.1016/j.rser.2007.01.023

[2] M. Ding, T. Liu, Y. Zhang, *Ionics* **26** (2020) 3415–3423. https://doi.org/10.1007/s11581-019-03425-3
[3] G. Kear, A. A. Shah, F. C. Walsh, *International Journal of Energy Research* **36** (2012) 1105–1120. https://doi.org/10.1002/er.1863
[4] Q. Xu, T. S. Zhao, C. Zhang, *Electrochimica Acta* **142** (2014) 61–67. https://doi.org/10.1016/j.electacta.2014.07.059
[5] A. Bhattarai, N. Wai, R. Schweiss, A. Whitehead, T. M. Lim, H. H. Hng, *Journal of Power Sources* **341** (2017) 83–90. https://doi.org/10.1016/j.jpowsour.2016.11.113
[6] A. Parasuraman, T. M. Lim, C. Menictas, M. Skyllas-Kazacos, *Electrochimica Acta* **101** (2013) 27–40. https://doi.org/10.1016/j.electacta.2012.09.067
[7] M. H. Chakrabarti, N. P. Brandon, S. A. Hajimolana, F. Tariq, V. Yufit, M. A. Hashim, *Journal of Power Sources* **253** (2014) 150–166. https://doi.org/10.1016/j.jpowsour.2013.12.038
[8] O. Di Blasi, N. Briguglio, C. Busacca, M. Ferraro, V. Antonucci, A. Di Blasi, *Applied Energy* **147** (2015) 74–81. https://doi.org/10.1016/j.apenergy.2015.02.073
[9] G. Qiu, A.S. Joshi, C.R. Dennison, K.W. Knehr, E.C. Kumbur, Y. Sun, *Electrochimica Acta* **64** (2012) 46–64. https://doi.org/10.1016/j.electacta.2011.12.065
[10] G, Qiu, C.R. Dennison, K.W. Knehr, E.C Kumbur, Y. Sun, *Journal of Power Sources* **219** (2012) 223–234. https://doi.org/10.1016/j.jpowsour.2012.07.042
[11] Q. Xu, T. S. Zhao, *Progress in Energy and Combustion Science* **49** (2015) 40–58. https://doi.org/10.1016/j.pecs.2015.02.001
[12] Q. Zheng, H. Zhang, F. Xing, X. Ma, X. Li, G. Ning, *Applied Energy* **113** (2014) 1675–1685. https://doi.org/10.1016/j.apenergy.2013.09.021
[13] Q. Xu, T. S. Zhao, C. Zhang, *Electrochimica Acta* **142** (2014) 61–67. https://doi.org/10.1016/j.jpowsour.2015.08.041
[14] M. Messaggi, P. Canzi, R. Mereu, A. Baricci, F. Inzoli, A. Casalegno, M. Zago, *Applied Energy* **228** (2018) 1057–1070. https://doi.org/10.1016/j.apenergy.2018.06.148
[15] J. Houser, A. Pezeshki, J. T. Clement, D. Aaron, M. M. Mench, *Journal of Power Sources* **351** (2017) 96–105. https://doi.org/10.1016/j.jpowsour.2017.03.083
[16] E. Knudsen, P. Albertus, K.T. Cho, A.Z. Weber, A. Kojic, *Journal of Power Sources* **299** (2015) 617–628. https://doi.org/10.1016/j.jpowsour.2015.08.041
[17] X. Y. Ke, J. M. Prahl, J. I. D. Alexander, R. F. Savinell, *Electrochimica Acta* **223** (2017) 124–134. https://doi.org/10.1016/j.electacta.2016.12.017
[18] X. Y. Ke, J. M. Prahl, J. I. D. Alexander, R. F. Savinell, *Journal of Power Sources* **384** (2018) 295–302. https://doi.org/10.1016/j.jpowsour.2018.03.001
[19] X. You, Q. Ye, P. Cheng, *International Communications of Heat and Mass Transfer* **75** (2016) 7–12. https://doi.org/10.1016/j.icheatmasstransfer.2016.03.021
[20] S. Maurya, P.T. Nguyen, Y. S. Kim, Q. Kang, R. Mukundan, *Journal of Power Sources* **404** (2018) 20–27. https://doi.org/10.1016/j.jpowsour.2018.09.093
[21] R. Gundlapalli, S. Jayanti, *Journal of Energy Storage* **30** (2020) 101516. https://doi.org/10.1016/j.est.2020.101516
[22] Y. Li, X. Zhang, J. Bao, M. Skyllas-Kazacos, *Journal of Energy Storage* **11** (2017) 191–199. https://doi.org/10.1016/j.est.2017.02.008
[23] X. Wu, X. Yuan, Z. Wang, J. Liu, Y. Hu, Q. Deng, X. Yin, Q. Zhou, W. Zhou, Y. Wu, *Journal of Solid State Electrochemistry* **21** (2017) 429–435. https://doi.org/10.1007/s10008-016-3361-x
[24] D.-J. Park, K.-S. Jeon, C.-H. Ryu, G.-J. Hwang, *Journal of Industrial and Engineering* Chemistry **45** (2017) 387–390. https://doi.org/10.1016/j.jiec.2016.10.007
[25] M. M. Tomadakis, T. J. Robertson, *Journal of Composite Materials* **39** (2005) 163-168. https://doi.org/10.1177/0021998305046438

[26] D. You, H. Zhang, J. Chen, *Electrochimica Acta* **54** (2009) 6827–6836. https://doi.org/10.1016/j.electacta.2009.06.086
[27] B. W. Zhang, Y. Lei, B. F. Bai, A. Xu, T. S. Zhao, *Applied Thermal Engineering* **151** (2019) 495–505. https://doi.org/10.1016/j.applthermaleng.2019.02.037
[28] J. T. Gostick, M. W. Fowler, M. D. Pritzker, M. A. Ioannidis, L. M. Behra, *Journal of Power Sources* **162** (2006) 228–238. https://doi.org/10.1016/j.jpowsour.2006.06.096
[29] A.Z. Weber, M.M. Mench, J.P. Meyers, P.N. Ross, J.T. Gostick, Q. Liu, *Journal of Applied Electrochemistry* **41** (2011) 1137. https://doi.org/10.1007/s10800-011-0348-2
[30] T. Jyothi Latha, S. Jayanti, *Journal of Power Sources* **248** (2014) 140–146. https://doi.org/10.1016/j.jpowsour.2013.09.084
[31] P. Leung, X. Li, C. Ponce de León, L. Berlouis, C. T. J. Low, F. C. Walsh, *RSC Advances* **2(27)** (2012) 10125-10156. https://doi.org/10.1039/C2RA21342G
[32] A. Tang, J. Bao, M. Skyllas-Kazacos, *Journal of Power Sources* **248** (2014) 154–162. https://doi.org/10.1016/j.jpowsour.2013.09.071
[33] S. Kumar and S. Jayanthi, *Journal of Power Sources* **307** (2016) 782–787. https://doi.org/10.1016/j.jpowsour.2016.01.048
[34] R. M. Darling, M. L. Perry, *Journal of The Electrochemical Society* **161** (2014) A1381–A1387. https://doi.org/10.1149/2.0941409jes